2nd Advanced Optical Metrology Compendium

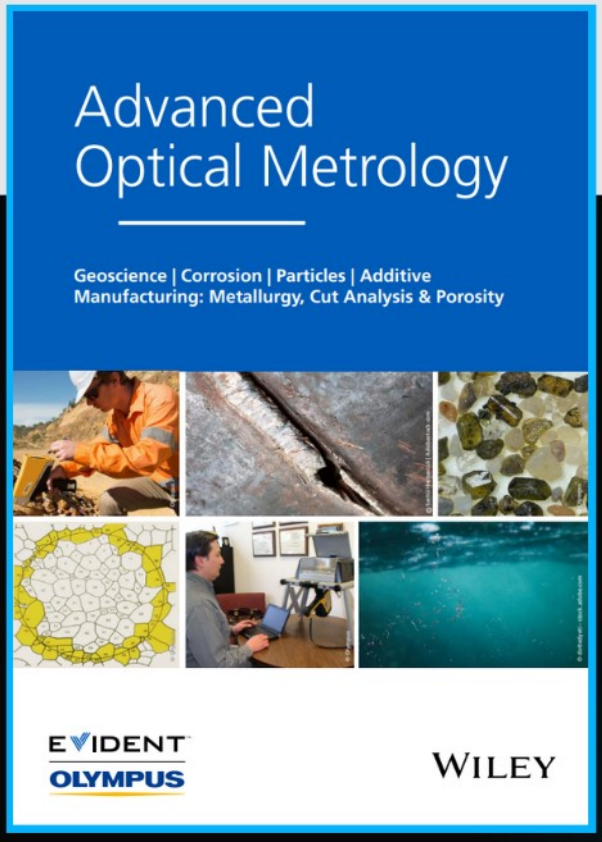

The latest eBook from Advanced Optical Metrology. Download for free.

This compendium includes a collection of optical metrology papers, a repository of teaching materials, and instructions on how to publish scientific achievements.

With the aim of improving communication between fundamental research and industrial applications in the field of optical metrology we have collected and organized existing information and made it more accessible and useful for researchers and practitioners.

EVIDENT
OLYMPUS

WILEY

NANO · MICRO small
www.small-journal.com

High Energy Capacitors Based on All Metal-Organic Frameworks Derivatives and Solar-Charging Station Application

Xijun Wei, Wanping Hu, Huarong Peng, Yuli Xiong, Peng Xiao, Yunhuai Zhang, and Guozhong Cao**

High energy and efficient solar charging stations using electrochemical capacitors (ECs) are a promising portable power source for the future. In this work, two kinds of metal-organic framework (MOF) derivatives, NiO/Co_3O_4 microcubes and Fe_2O_3 microleaves, are prepared via thermal treatment and assembled into electrochemical capacitors, which deliver a relatively high specific energy density of 46 Wh kg^{-1} at 690 W kg^{-1}. In addition, a solar-charging power system consisting of the electrochemical capacitors and monocrystalline silicon plates is fabricated and a motor fan or 25 LEDs for 5 and 30 min, respectively, is powered. This work not only adds two novel materials to the growing categories of MOF-derived advanced materials, but also successfully achieves an efficient solar-ECs system for the first time based on all MOF derivatives, which has a certain reference for developing efficient solar-charge systems.

1. Introduction

Solar energy is readily available and the most abundant renewable resources on the earth, however, given the intermittent nature of solar energy, designing efficient solar charge–discharge system is one of the main trends for green energy development in the future.[1–3] Recently, some research have investigated solar charging system,[4–6] which is composed by solar cell and energy storage device. One of the critical issues needs to be addressed for efficient solar charging system is the power matching principle. High power solar cell should be matched with a high power energy storage device, this is why electrochemical capacitor (EC) is often used as energy storage device in this system.[7–12] Electrochemical capacitor has promising application foreground in this system due to its high specific power density, fast charging/discharging process, and long cycling life.[13–18] For example, Karthik and co-workers assembled a self-sustaining power station by combining the electrochemical double-layer capacitors (EDLCs) and a commercial solar cell, which exhibited an energy density of 17.7 Wh kg^{-1} and could power 40 light-emitting diodes after charging.[19] However, because of the low specific energy density of ECs, the solar-ECs system usually has low discharging durability. Therefore, in the past decade, many researchers have devoted on increasing the energy density without sacrificing other properties of ECs by designing new system and developing advanced electrode materials.[20–26]

Prussian blue (PB) and its analogs (PBAs) with a general chemical formula $M_3^{II}[M^{III}(CN)_6]_2 \cdot nH_2O$ (M = Mn, Co, Ni, Fe, etc.)[27–29] belong to one kind of metal-organic frameworks (MOFs) and are extensively used as promising precursors to manufacture complex structure metal oxides. Compared with other fabrication approaches, the morphology and pore structure of the metal oxides derivatives can be regulated by controlling the annealing temperature, rate and time, since lots of ligands binding to the metal ions in the precursors may create gases during the annealing. The derived transition metal oxides have been used for various catalytic reaction, energy conversion and storage, molecular magnets, and sensors.[30–36] More importantly, PB/PBAs derivatives have received greatly interest for the electrochemical energy storage due to their novel pore structure, which is beneficial for ion transport. For example, Lou and co-workers synthesized a series of Fe_2O_3 microboxes by annealing PB microcubes at different temperatures (350 °C, 550 °C and 650 °C), the hierarchical Fe_2O_3 microboxes (650 °C) showed the highest capacity of 950 mAh g^{-1} at 200 mA g^{-1} because of the hierarchical shell and hollow structure that facilitate the permeation of electrolyte and the transmission of lithium ions.[37] Wang and co-workers proposed an innovative approach to prepare the hollow structure PBA submicroboxes (CoHCF), when used as anode in hybrid supercapacitor,

Dr. X. J. Wei, Dr. W. P. Hu, Dr. H. R. Peng, Prof. Y. H. Zhang
College of Chemistry and Chemical Engineering
Chongqing University
Chongqing 400044, P. R. China
E-mail: zyh2031@cqu.edu.cn
Dr. Y. L. Xiong, Prof. P. Xiao
College of Physics
Chongqing University
Chongqing 400044, P. R. China
Prof. G. Z. Cao
Department of Materials Science and Engineering
University of Washington
Seattle, WA 98195, USA
E-mail: gzcao@uw.edu
The ORCID identification number(s) for the author(s) of this article can be found under https://doi.org/10.1002/smll.201902280.

DOI: 10.1002/smll.201902280

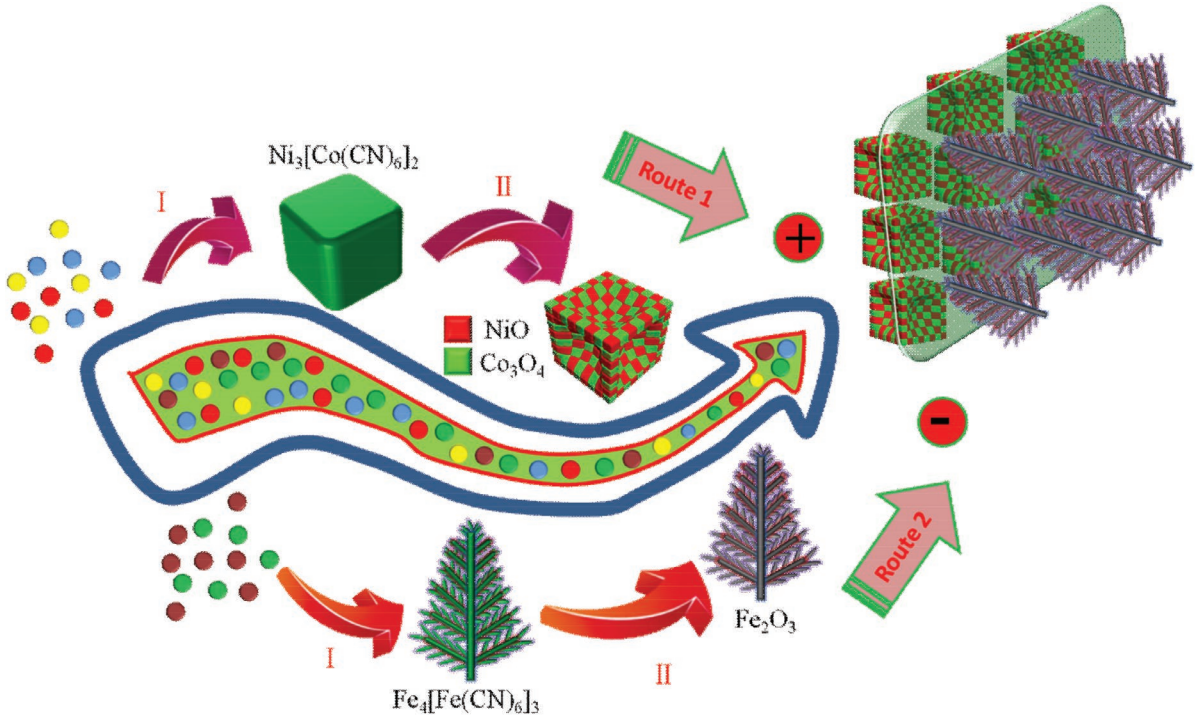

Scheme 1. Schematic illustration of the preparation processes of NiO/Co_3O_4 microcubes and Fe_2O_3 microleaves. Route 1: (I) fabrication of $Ni_3[Co(CN)_6]_2$ microcubes; (II) preparation of NiO/Co_3O_4 microcubes by heat treatment of the precursors; Route 2: (I) fabrication of $Fe_4[Fe(CN)_6]_3$ microleaves; (II) preparation Fe_2O_3 microleaves by heat treatment of the precursors. Finally, they are assembled into an electrochemical capacitor as cathode and anode materials, respectively.

the device exhibited a high energy density of 42.5 Wh kg^{-1} at 21.1 kW kg^{-1} due to the unique hollow structure with defined mesoporosity that allow efficient electrolyte diffusion/penetration and enlarge the electrolyte/electrode interface.[28] In our previous work, Co_3O_4/Fe_2O_3 mixed metal oxides derived from $Co_3[Fe(CN)_6]_2 \cdot 10H_2O$ were prepared and used for symmetric supercapacitors, the structure and compositional advantages made the device presented an energy density of 35.15 Wh kg^{-1} at 1125 W kg^{-1}.[38] Therefore, all evidences demonstrated that PB/PBAs derivatives had promising prospect for ECs and batteries application with high energy density. However, for constructing a high energy density ECs, one crucial thing is that the positive and negative electrodes must have matchable capacitance. At present, many research mainly focused on cathode materials and finding the suitable anode materials to couple with the cathode materials is still a great challenge.

Here, we present an electrochemical capacitor based on all MOFs derivatives according to the matching principle. Fe_2O_3 microleaves (FM) and concave surface NiO/Co_3O_4 microcubes (NCM) with unique pore structure are prepared via controlled pyrolyzing PB ($Fe_4[Fe(CN)_6]_3$) and PBA ($Ni_3[Co(CN)_6]_2$), respectively. The electrochemical capacitor $NiO/Co_3O_4//Fe_2O_3$ (NCM//FM) demonstrates a 1.4 V window potential, a relatively high energy density of 46 Wh kg^{-1} at 690 W kg^{-1} and excellent cycling performance. Moreover, we assemble a solar-ECs power station to harvest solar energy. The assembled solar-ECs station can efficiently charge the NCM//FM device and the stored charge could operate a toy motor fan or 25 LEDs, signifying the prospect of our solar-ECs station in practical application. In general, we successfully add two novel materials to the growing categories of MOF-derived advanced materials and a solar-ECs power station with high energy density is fabricated based on all MOF derivatives for the first time.

2. Results and Discussion

2.1. Physicochemical Characterization

The fabrication procedures of Fe_2O_3 microleaves and NiO/Co_3O_4 microcubes are schematically illustrated in **Scheme 1**. Route 1 shows the preparation of $Ni_3[Co(CN)_6]_2$ precursors via a wet-chemical method and then thermal treatment of the obtained products in air at 300 °C for 1 h and 450 °C for 2 h to get concave NiO/Co_3O_4 microcubes. Route 2 demonstrates the preparation of $Fe_4[Fe(CN)_6]_3$ precursors by a hydrothermal method and then annealing above precursors in air at 450 °C for 3 h to get Fe_2O_3 microleaves. Figure S1 (Supporting Information) exhibits the obtained XRD patterns of the NiO/Co_3O_4 microcubes and Fe_2O_3 microleaves. The diffraction peaks of the NiO/Co_3O_4 microcubes at 31.27°, 37.24°, 44.80°, 59.35° and 65.23° can be readily assigned to the (220), (311), (400), (511), and (440) crystal planes of Co_3O_4 (JCPDS card #43-1003); other peaks at 37.24°, 43.27°, 62.87°, 75.41° and 79.40° are corresponding to the crystal planes of (111), (200), (220), (311), and (222) of NiO (JCPDS card #47-1049). For Fe_2O_3 microleaves, all diffraction peaks are matched well with Fe_2O_3 phase (JCPDS card #42-1467), which suggests that $Fe_4[Fe(CN)_6]_3$ precursors

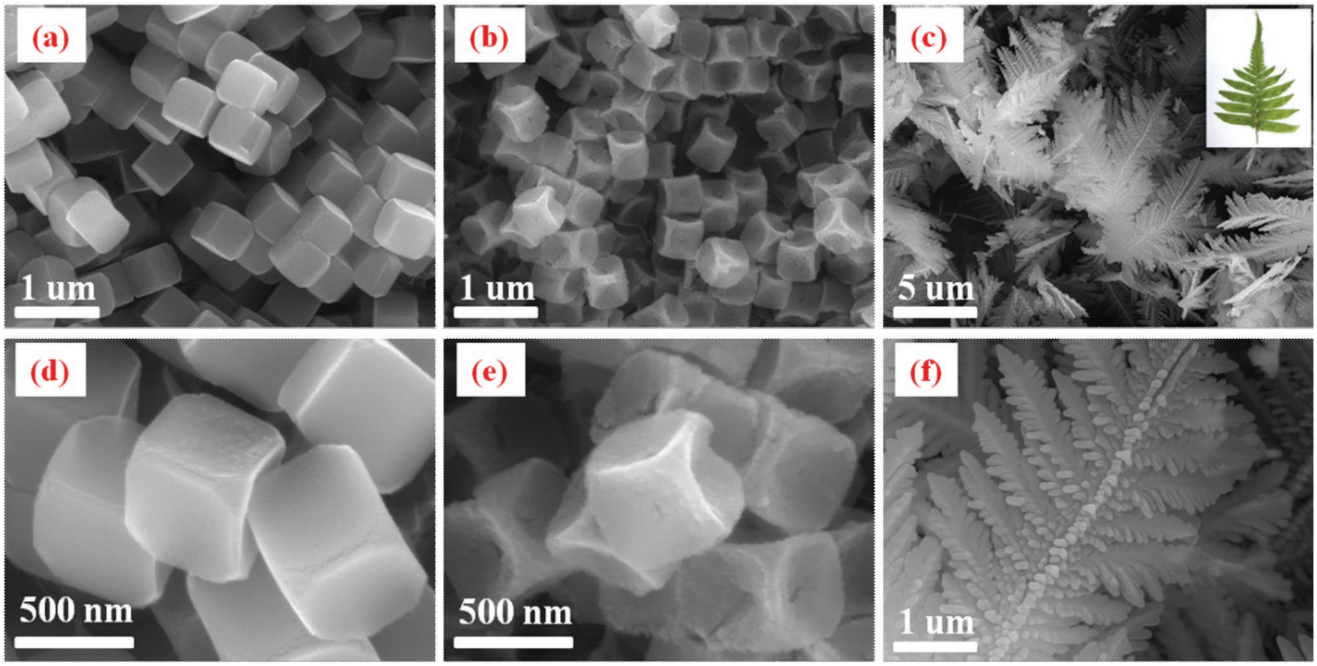

Figure 1. a,d) FESEM images of the precursor $Ni_3[Co(CN)_6]_2$ at different magnification; b,e) FESEM images of NiO/Co_3O_4 microcubes at different magnification; c,f) FESEM images of Fe_2O_3 microleaves at different magnification, respectively.

were converted into Fe_2O_3 completely. Figure S2a,b (Supporting Information) shows the individual XRD patterns of the two precursors, corresponding to the JCPDS card #89-3738 and JCPDS card #73-0687.

The FESEM images as shown in **Figure 1**a,d and Figure S3a (Supporting Information) revealed that $Ni_3[Co(CN)_6]_2$ particles are uniform in size with diameters ≈400–500 nm with smooth surface. After pyrolysis, NiO/Co_3O_4 microcubes were formed, which maintained the precursor's morphology with cube faces becoming concave, as shown in Figure 1b, e and Figure S3b (Supporting Information), as a result of decomposition and volatilization of organic compounds. The SEM image of $Fe_4[Fe(CN)_6]_3$ in Figure S3c (Supporting Information) revealed leaves-like morphology with very uniform size distribution. After pyrolysis, resulting Fe_2O_3 retained the microleave shape, as shown in Figure 1c,f and Figure S3d (Supporting Information). TEM images of NiO/Co_3O_4 microcubes (**Figure 2**a,b) show clearly the hollow structure, and HRTEM image in Figure 2c shows clear lattice fringes of 0.24 and 0.28 nm corresponding to the (311) and (220) crystal planes of spinel Co_3O_4, and 0.21 and 0.24 nm corresponding to the (200) and (111) crystal planes of cubic NiO, respectively. Figure 2d shows the element mapping of NiO/Co_3O_4 microcubes that obtained by a high-angle annular dark field TEM (HAADF-TEM), confirming the uniform distributing of Ni, Co, O, and C elements. TEM images of Fe_2O_3 microleaves are shown in Figure 2e,f and the HRTEM image in Figure 2g exhibits the lattice fringe of 0.25 nm for (311) plane of Fe_2O_3. The element mapping of Fe_2O_3 microleaves that obtained by HAADF-TEM shown in Figure 2h, confirming that Fe, O, and C elements are uniform distributed in Fe_2O_3 microleaves. The metal oxides, NiO/Co_3O_4 microcubes and Fe_2O_3 microleaves, derived from MOFs could maintain the morphology of their precursors through pyrolysis, which is benefit to construct the unique advanced materials. It is noted that there are some trace of carbon residual in the resulting oxides; such trace carbon residual may increase the electrical conductivity of the metal oxides and affect the surface chemistry of the oxides.

The chemical states and elemental composition of NiO/Co_3O_4 microcubes and Fe_2O_3 microleaves are characterized by XPS analysis. In Figure S5a (Supporting Information), the Ni $2p_{3/2}$ (854.4 eV) and Ni $2p_{1/2}$ (873.9 eV) orbits were observed.[39] Focusing on the Ni $2p_{3/2}$ state, it shows spin–orbit doublets that are belong to Ni^{2+} in the standard Ni–O octahedral bonding configuration in cubic NiO and the vacancy-induced Ni^{2+} ion.[40,41] In Figure S5b (Supporting Information), the Co $2p_{3/2}$ and Co $2p_{1/2}$ orbits with a splitting of 15.4 eV are observed at 779.2 and 794.6 eV along with two shakeup satellites, revealing the coexistence of Co^{3+} and Co^{2+} in Co_3O_4.[42] Furthermore, as shown in Figure S5c (Supporting Information), Fe $2p_{3/2}$ and Fe $2p_{1/2}$ orbits with a splitting of 13.4 eV were observed at 711 and 724.6 eV, which confirm the presence of Fe^{3+}.[43,44] Figure S6a (Supporting Information) shows the O 1s spectra of NiO/Co_3O_4 microcubes, the peak of O1 at 529.2 eV represents the typical metal–oxygen bond, the peak of O2 at 531.1 eV corresponds to the hydroxyl group (−OH) on the surfaces of NiO/Co_3O_4, and the peak of O3 at 532.5 eV can be ascribed to chemically and physically adsorbed water on the material surface.[41,45] As for Fe_2O_3 microleaves, the peak observed at 529.3 eV correlates to Fe−O bond, the peak observed at 531.3 eV represents the −OH on the surfaces of Fe_2O_3 and the peak at 532.7 eV can be ascribed to the adsorbed water on the Fe_2O_3 surface,[44,45] as shown in Figure S6b (Supporting Information). Figure S6c,d (Supporting Information) shows the C 1s spectra of NiO/Co_3O_4 microcubes and Fe_2O_3 microleaves. As for NiO/Co_3O_4

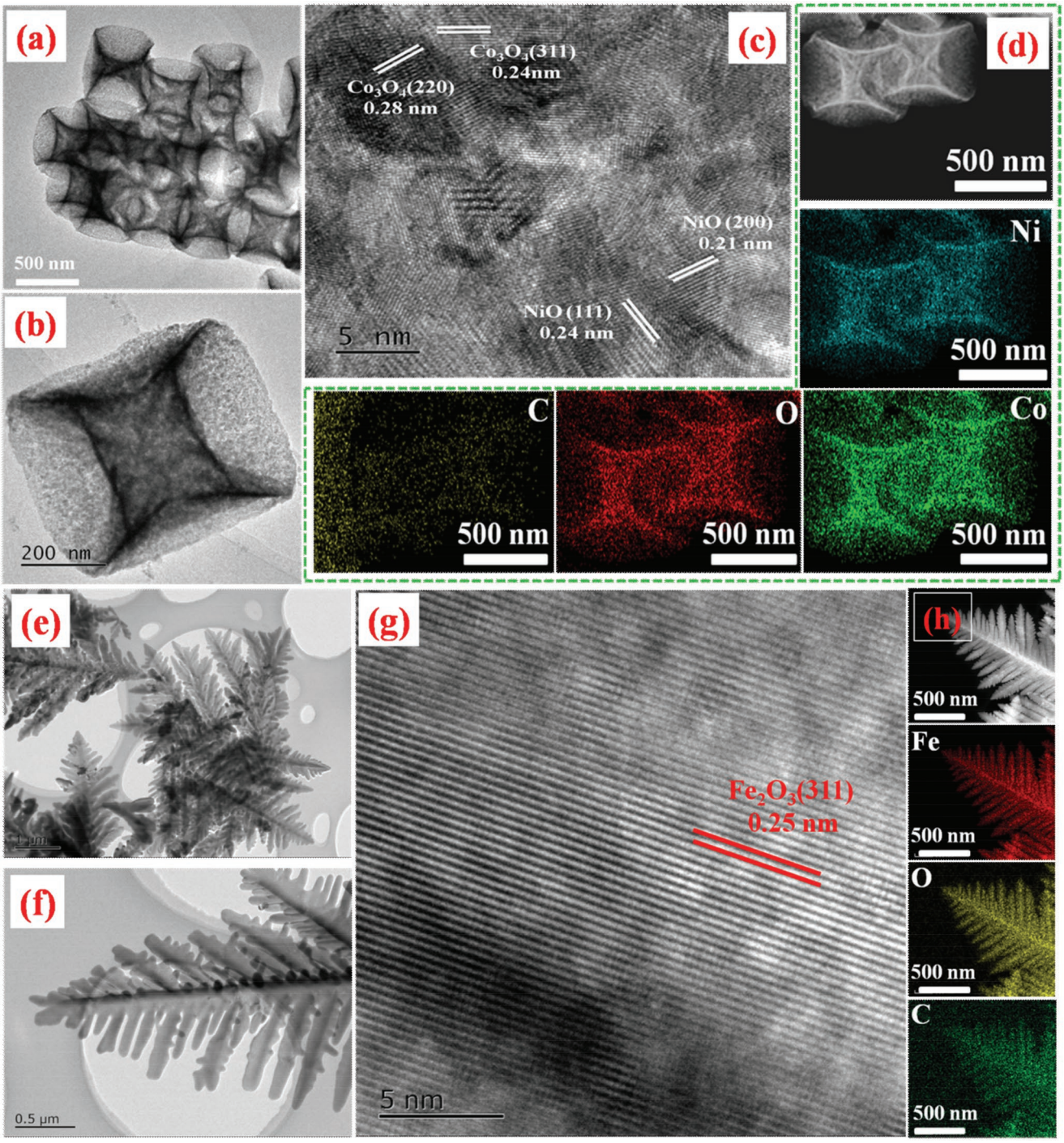

Figure 2. a,b) TEM images of the NiO/Co_3O_4 microcubes at different magnification; c) HRTEM image of the NiO/Co_3O_4 microcubes; d) HAADF-STEM image and corresponding EDX elemental mappings for Ni, Co, O, and C of the NiO/Co_3O_4 microcubes, respectively; e,f) TEM images of the Fe_2O_3 microleaves at different magnification; g) HRTEM image of the Fe_2O_3 microleaves; h) HAADF-STEM image and corresponding EDX elemental mappings for Fe, O, and C of the Fe_2O_3 microleaves, respectively.

microcubes, the peak at 284.1 eV corresponds to the C=C bond, and the peaks at 286.1 and 288.3 eV can be assign to the C—O and C=O bonds respectively; the peaks at 284.5, 286.2, and 288.4 eV of Fe_2O_3 microleaves are belong to the C=C, C—O, C=O bonds respectively, which caused by the carbon residual from the organic components during pyrolysis.[38]

The N_2 adsorption/desorption isotherms test was performed to estimate the Brunauer–Emmett–Teller (BET)-specific surface area of the Fe_2O_3 microleaves and NiO/Co_3O_4 microcubes, respectively. Fe_2O_3 microleaves exhibits a typical IV-type isotherms with H3-type hysteresis loop and the obtained specific surface is 64.2 m^2 g^{-1} (Figure S7a, Supporting Information)

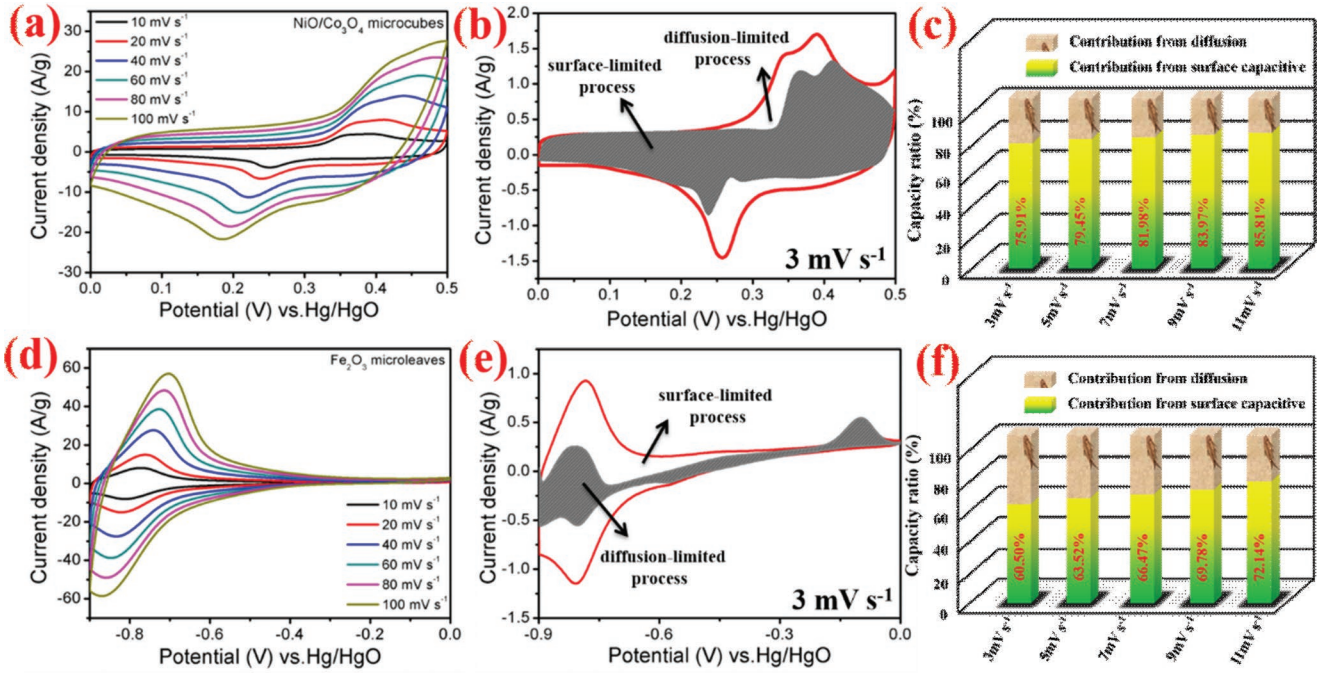

Figure 3. a,d) Cyclic voltammogram curves of NiO/Co_3O_4 microcubes and Fe_2O_3 microleaves at 10– 100 mV s^{-1}, respectively; b,e) surface-limited (the gray area) and diffusion-limited (the white area) charge storage contributions separated for NiO/Co_3O_4 microcubes and Fe_2O_3 microleaves at 3 mV s^{-1}, respectively; c,f) histograms for comparison of capacity ratio of diffusion-controlled and surface capacitive charge for NiO/Co_3O_4 microcubes and Fe_2O_3 microleaves at 3–11 mV s^{-1}, respectively.

with pore distribution in the range of 2.4–3.4 nm (Figure S7b, Supporting Information). NiO/Co_3O_4 microcubes exhibit a typical IV-type isotherms with H1-type hysteresis loop with a specific surface of 102.6 m^2 g^{-1} (Figure S7c, Supporting Information) with pores in the range of 4.2–6.3 nm (Figure S7d, Supporting Information). The specific surface areas of our samples are higher than that of the Fe_2O_3 and Ni–Co oxides reported in literature (summarized in Table S1, Supporting Information).

2.2. Energy Storage Performance

The electrochemical energy storage behavior of NiO/Co_3O_4 microcubes and Fe_2O_3 microleaves were tested using a three-electrode equipment. **Figure 3**a,d exhibits the CV curves of the NiO/Co_3O_4 microcubes and Fe_2O_3 microleaves at 10–100 mV s^{-1}, respectively. In Figure 3a, the CV curves of NiO/Co_3O_4 microcubes are similar to the rectangle with redox peaks, which indicates that both pseudocapacitance (redox reaction of nickel and cobalt with OH^-) and electric double-layer capacitance (charge stored at the double-layer interface) are contributed to the total capacitance. The oxidation peak of 0.35 and 0.4 V at 10 mV s^{-1} are belong to Co_3O_4 and NiO respectively, and the reduction peaks of the two components are combined at 0.25 V.[46,47] The shape of CV curves change little and the area enclosed increases with the increasing of scan rate, this demonstrates that the NiO/Co_3O_4 microcubes have good electrical conductivity and reversibility. For Fe_2O_3 microleaves negative electrode, the CV curves (Figure 3d) display apparent redox peaks, demonstrating the total capacitance is mainly contributed by redox reaction between Fe^{2+} and Fe^{3+} associated with OH^-.[48] The corresponding oxidation and reduction peaks shift little with the scan rate increasing, exhibiting the Fe_2O_3 microleaves have good reaction kinetics. As shown in Figure S8a,c (Supporting Information), the electrochemically active surface area (ECSA) of NiO/Co_3O_4 microcubes and Fe_2O_3 microleaves were evaluated via a CV method, where the ECSA could be represented by the linear slope (twice of the electrochemical double-layer capacitance, C_{dl}). In Figure S8b,d (Supporting Information), by calculating the slope from the linear relationship of the current density against the scan rate, C_{dl} of NiO/Co_3O_4 microcubes is confirmed to be 280.4 mF cm^{-2}, which is much higher than that of Fe_2O_3 microleaves (C_{dl} = 95.5 mF cm^{-2}. Due to the larger ECSA that NiO/Co_3O_4 microcubes show apparent double-layered capacitance. For further investigate the charge storage mechanism and reaction kinetic of the two materials, CV tests were performed at 3–11 mV s^{-1} (Figure S9a,b, Supporting Information). Using Dunn's method, the total charge storage of NiO/Co_3O_4 microcubes and Fe_2O_3 microleaves is divided into two parts: diffusion-controlled contribution and near-surface capacitive contribution.[49] The diffusion-controlled contribution improves the energy density and the near-surface capacitive contribution benefits the high power density. In Figure 3b,e, the gray-shaded regions represent the contribution from surface capacitive of the two materials, respectively. Figure 3c,f shows the contribution ration of the surface capacitive and diffusion-controlled process at different scan rates, respectively. The estimated surface capacitive contribution of NiO/Co_3O_4 microcubes and Fe_2O_3 microleaves are about 75.91% and 60.50% of the total charge storage at 3 mV s^{-1}, respectively, and higher than diffusion-controlled contribution,

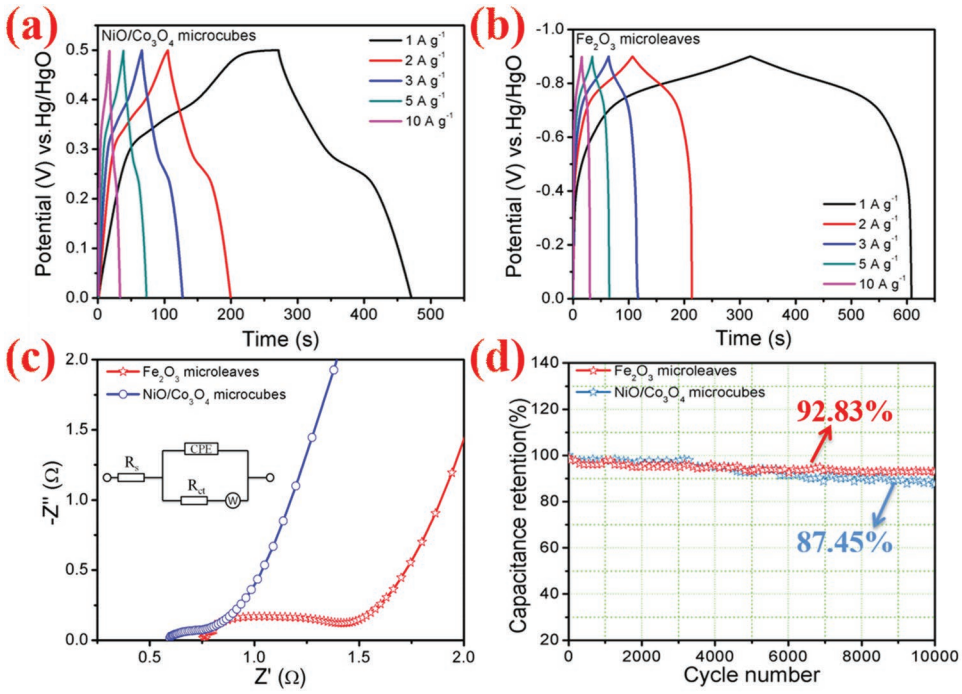

Figure 4. a,b) Charge–discharge curves of NiO/Co_3O_4 microcubes and Fe_2O_3 microleaves at 1–10 A g^{-1}, respectively; c) Nyquist plots of the microcubes and Fe_2O_3 microleaves and the inset exhibits the corresponding equivalent circuits; d) long cycling stability of NiO/Co_3O_4 microcubes and Fe_2O_3 microleaves, respectively.

which demonstrate effective surface charge storage of the two materials. With an increased scan rate, the percentage of surface capacitive contribution increased and diffusion-controlled contribution decreased.

Figure 4a,b exhibits the GCD curves of the two materials at different current densities. In Figure 4a, all the GCD curves of the NiO/Co_3O_4 microcubes show nonlinear curves with small ohmic drop. According to the discharge time, the specific capacitance of NiO/Co_3O_4 microcubes is 430, 400, 378, 350, and 337 F g^{-1} at the current densities of 1, 2, 3, 5, and 10 A g^{-1}. In Figure 4b, the GCD curves of Fe_2O_3 microleaves exhibit highly symmetry, demonstrating good reversibility. According to the discharge curves, the specific capacitance of Fe_2O_3 microleaves is 328, 267, 233, 194, and 178 F g^{-1} at the current densities of 1, 2, 3, 5, and 10 A g^{-1}. Furthermore, the gravimetric capacitance of Fe_2O_3 microleaves and NiO/Co_3O_4 microcubes were calculated to be 328 and 430 F g^{-1} at 1 A g^{-1}, respectively. The matching capacitances are beneficial for constructing ECs with high energy density. Moreover, EIS tests were carried out to further investigate the conductivity of the prepared materials from 100 kHz to 0.01 Hz and the results are presented in Figure 4c. The inset of Figure 4c shows the corresponding equivalent circuit diagram. According to the results, the charge-transfer resistant of NiO/Co_3O_4 microcubes and Fe_2O_3 microleaves are about 0.26 and 0.74 Ω, respectively, this result means that the NiO/Co_3O_4 microcubes have a better conductivity than Fe_2O_3 microleaves, consistent with GCD results above. The long time cycling life of NiO/Co_3O_4 microcubes and Fe_2O_3 microleaves were evaluated at 10 A g^{-1} and results are exhibited in Figure 4d. Obviously, the Fe_2O_3 microleaves show higher durability compare with NiO/Co_3O_4 microcubes and exhibit capacity retention of 92.83% and 87.45% of their initial capacitance, respectively. This is may be due to the intense reaction of NiO/Co_3O_4 microcubes caused by better conductivity, which lead to more serious damage to the electrode structure.

In **Figure 5**a, the separate CV measurements at 10 mV s^{-1} were performed for the two materials with different potential windows. Obviously, the NiO/Co_3O_4 microcubes and Fe_2O_3 microleaves showed matchable charge storage capability, which is very suitable for constructing high energy storage devices. Therefore, an electrochemical capacitor was constructed by using the NiO/Co_3O_4 microcubes and Fe_2O_3 microleaves as positive and negative electrode materials (NCM//FM), respectively. The package of our assembled device is illustrated in Figure 5b. The CV curves of our assembled capacitor with various upper cutoff potential of 1.1–1.5 V are shown in Figure S10 (Supporting Information), which demonstrate that the NCM//FM could achieve a large potential window up to 1.4 V without obvious polarization. The CV curves of as-assembled NCM//FM capacitor at different scan rates with 0–1.4 V are shown in Figure 5c. Obviously, the shape of CV curves is nonrectangular with weak redox peak, which suggest that the charge storage of NCM//FM combines the contribution of both pseudocapacitance and electrical double-layer capacitance. Meanwhile, the shape of the CV curves do not change and the area enclosed increases as the scan rates increased, which demonstrate the good electrical conductivity and rapid ions diffusion of the device.

Figure 5d shows the GCD curves of the device at 1–10 A g^{-1}. Obviously, the GCD curves are highly symmetrical with negligible ohmic drop, which confirms the good reversibility and low internal resistance of the device. Furthermore, the obtained

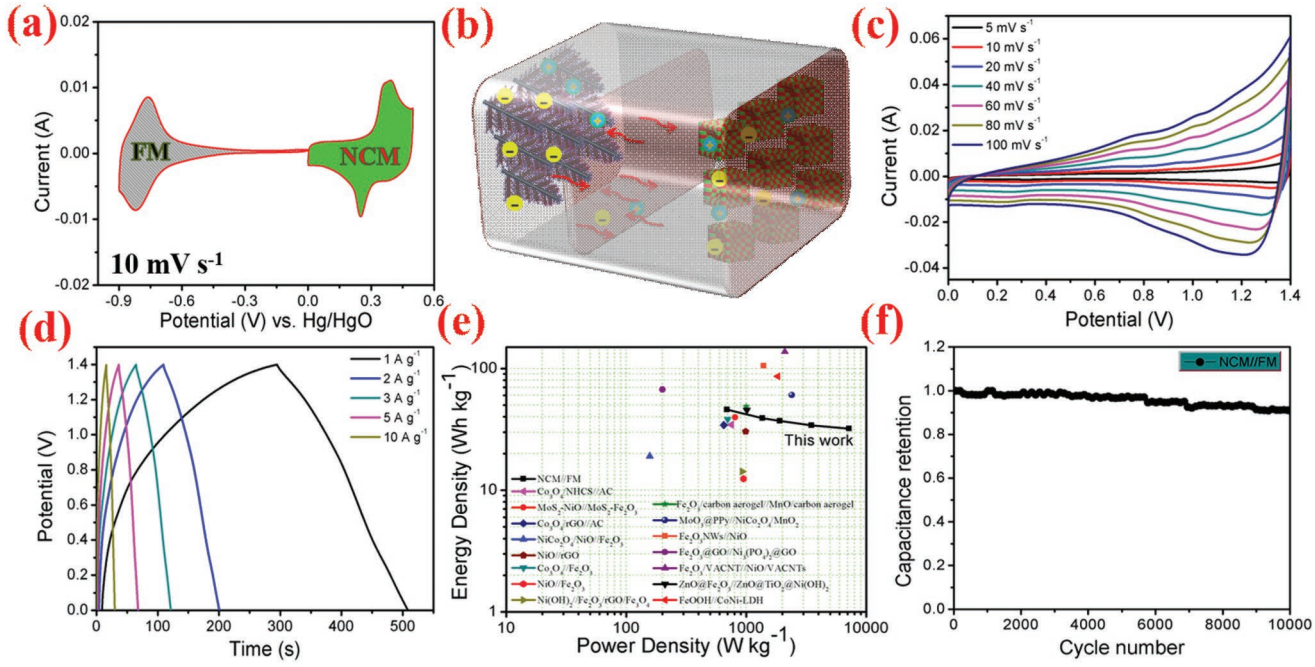

Figure 5. a) The separate cyclic voltammogram curves of NiO/Co_3O_4 microcubes and Fe_2O_3 microleaves electrodes at 10 mV s^{-1}; b) schematic illustration of our assembled device that using the NiO/Co_3O_4 microcubes and Fe_2O_3 microleavesas the anode and cathode, respectively; c,d) CV and GCD curves of the NCM//FM at 10–100 mV s^{-1} and 1–10 A g^{-1}; e) Ragone plots of as-assembled device compared with previous reported data about Ni–Co–Fe oxide-based devices; f) long cycling stability of the NCM//FM at 10 A g^{-1}.

NCM//FM device shows a specific capacitance of 171 F g^{-1} at 1 A g^{-1} and 70% retention of the initial capacitance even at 10 A g^{-1}, demonstrating the good rate capability. Moreover, because of reasonable cathode and anode matching, the as-prepared NCM//FM delivered a high energy density of 46 Wh kg^{-1} at 690 W kg^{-1}, this value is in the middle leave compared with the previously published ECs composed by Ni/Co/Fe-based metal oxides or compounds fabricated by general chemical methods. Figure 5e shows the Ragone plots of our device comparing to other devices, including MoS_2–NiO//MoS_2-Fe_2O_3 (39.6 Wh kg^{-1}),[40] $NiCo_2O_4$/NiO//Fe_2O_3 (19 Wh kg^{-1}),[50] Co_3O_4//Fe_2O_3 (38.1 Wh kg^{-1}),[51] Co_3O_4/NHCS//AC (34.5 Wh kg^{-1}),[52] NiO//Fe_2O_3 (12.4 Wh kg^{-1}),[53] NiO//rGO (30.3 Wh kg^{-1}),[54] Co_3O_4/rGO//AC (34.3 Wh kg^{-1}),[55] $Ni(OH)_2$//Fe_2O_3/rGO/Fe_3O_4 (14.2 Wh kg^{-1}),[56] Fe_2O_3/carbon aerogel//MnO/carbon aerogel (48.7 Wh kg^{-1}),[57] MoO_3@PPy//$NiCo_2O_4$/MnO_2 (60.4 Wh kg^{-1}),[58] Fe_2O_3 NWs//NiO (105 Wh kg^{-1}),[59] Fe_2O_3@GO//$Ni_3(PO_4)_2$@GO (67.2 Wh kg^{-1}),[60] FeOOH//CoNi–LDH (86.4 Wh kg^{-1}),[61] Fe_2O_3/VACNT//NiO/VACNTs (137.3 Wh kg^{-1}),[62] and ZnO@Fe_2O_3//ZnO@TiO_2@$Ni(OH)_2$ (52.2 Wh kg^{-1}).[63] This indicates that the metal oxide derivatives of MOFs can be applied for high energy density storage device due to their special structure. Furthermore, due to the better capacitance matching of our prepared positive and negative electrode materials that the obtained energy density is higher than other ECs, which is constructed by using MOFs derivatives as positive electrode and carbon-based materials as negative electrode (36–41.65 Wh kg^{-1}).[47,64–66] Moreover, the assembled device can deliver 32 Wh kg^{-1} even at 7200 W kg^{-1}, demonstrating that the NCM//FM can exhibit the high energy density and power density simultaneously. The cycling life of our fabricated NCM//FM was examined by repetitive charge–discharge process at 10 A g^{-1} (Figure 5f), the result shows excellent long cycling life with only 9.2% capacitance attenuation after 10000th cycles as compared to its initial value.

To further verifying the practicability of our prepared NCM//FM electrochemical capacitor, a solar-charging power system was assembled. **Scheme 2** depicts the corresponding solar-ECs charging system consisting of two NCM//FM electrochemical capacitors in series which were attached to the three monocrystalline silicon plates in parallel. **Figure 6**a shows the components of the solar-ECs system. According to the Figure 6b, it can be seen that the voltage between the two NCM//FM devices rises to 2.87 V after charging for 20 s by the silicon plates under the simulated solar light source. The letters of "CQU" consisted of 25 LEDs, as the energy-consuming part,

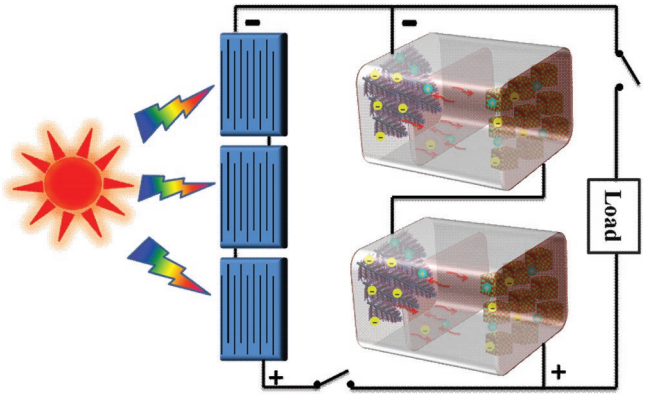

Scheme 2. Schematic illustration of the solar-ECs charging device.

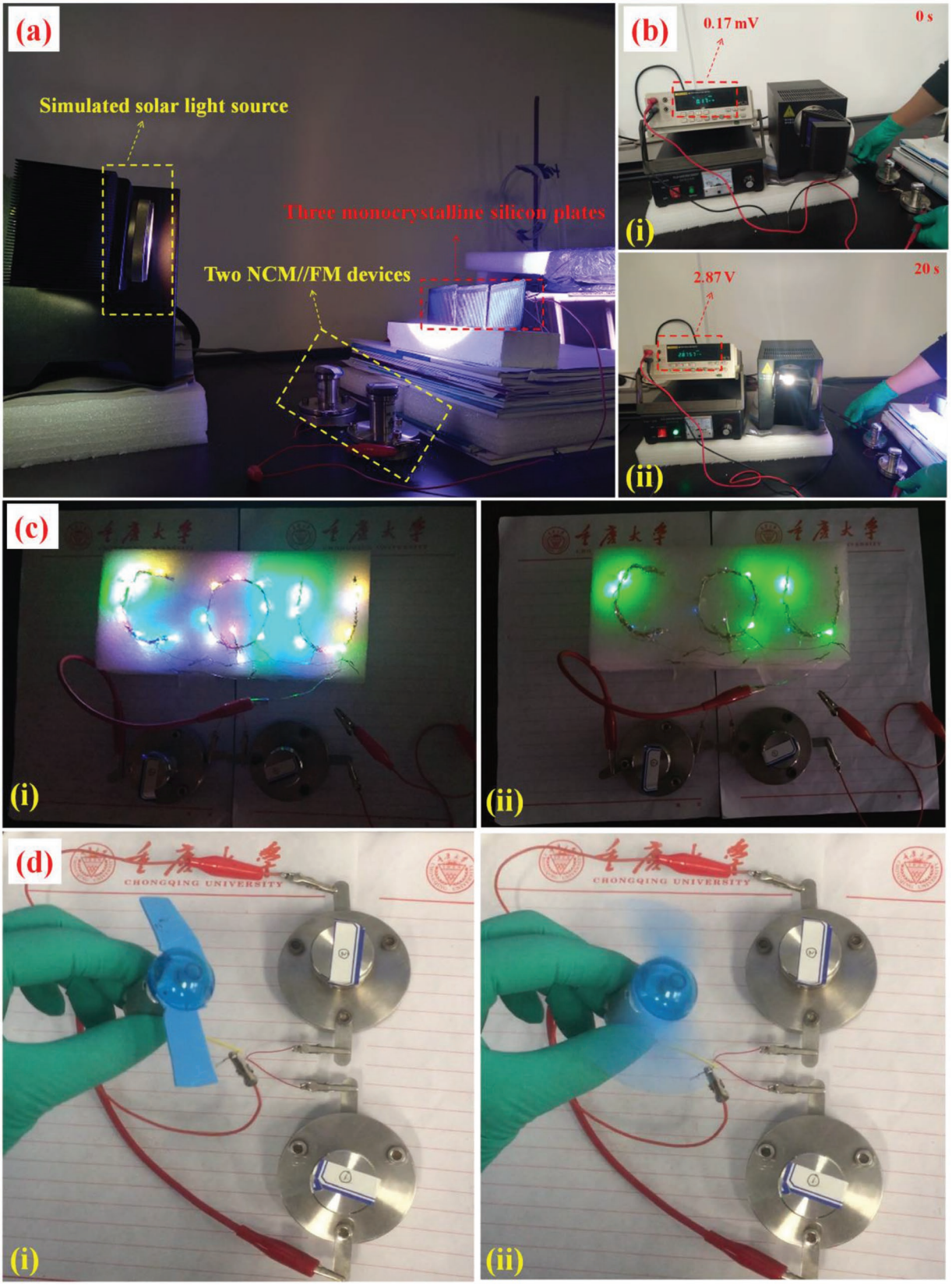

Figure 6. a) The components of the self-charging power station; b) photographic images of the silicon plate charges to the NCM//FM through the simulated solar light source; c) lighting 25 LEDs with "CQU" display for about 30 min; d) driving a toy motor fan for around 5 min.

were connected to the two NCM//FM devices after charging completed, the devices can light the LEDs for nearly 30 min, as shown in Figure 6c. Moreover, two fully charged NCM//FM can drive a toy motor fan successfully for ≈5 min, as shown in Figure 6d. In general, this solar-ECs system is a proof of concept evidences that our prepared NCM//FM electrochemical capacitor with high energy density is suitable for solar-charging system.

3. Conclusion

An electrochemical capacitor with high energy density was fabricated on the basis of all MOF derivatives at the first time and the $NiO/Co_3O_4//Fe_2O_3$ capacitor delivered a high energy density of 46 Wh kg^{-1} at 690 W kg^{-1}. The high energy density is mainly ascribed to the unique structure of the metal oxides with high specific surface area and highly porous, which possess much increased reaction active sites and accelerated the transport rate of ions and electrons. In addition, the trace carbon in MOF derivatives would increase the electrical conductivity and benefit the electron transport in the capacitors. Combining the capacitor with monocrystalline silicon, an efficient solar-charging station was successfully designed and demonstrate. The experimental results showed that the solar-charging station can power a motor fan or 30 LEDs for a long duration. Two novel materials were added to the growing categories of MOF-derived advanced materials, which have a promising application prospect in solar-charging system.

4. Experimental Section

Materials: $K_3[Fe(CN)_6]$ and $K_3[Co(CN)_6]$ were purchased from Sigma-Aldrich Co., Ltd. $Ni(NO_3)_2{\cdot}6H_2O$, $C_4H_6N_2$, CH_3CH_2OH, $Na_3C_6H_5O_7{\cdot}2H_2O$, and KOH were purchased from Aladdin Biological Technology. The monocrystalline silicon plates were purchased from Solar Tech Co., Ltd., China. The glass fiber filter paper was bought from Whatman Co., Ltd. All the chemicals were used directly without further treatment in the experiment.

Synthesis of $Ni_3[Co(CN)_6]_2$ (Ni-Co PBA) Precursors and NiO/Co_3O_4 Microcubes (NCM): Solution A: 1.3 g of sodium citrate and 0.8 g of nickel nitrate were dissolved in 20 mL of deionized water (DIW); Solution B: 1.6 g of potassium hexacyanocobaltate (III) was dissolved in 20 mL of DIW. First, mixing solutions A and B together under stirring at room temperature and aging for 24 h. Then, the green precipitates were collected by centrifugation, washed with DIW and ethanol for several times, and dried at 70 °C overnight. Finally, the obtained Ni–Co PBA precursors were annealed at 300 °C for 1 h and 450 °C for 2 h in air directly to obtain the NiO/Co_3O_4 microcubes.

Synthesis of $Fe_4[Fe(CN)_6]_3$ (Fe–Fe PB) Precursors and Fe_2O_3 Microleaves (FM): 1.3 g of sodium citrate and 1.5 g of potassium ferricyanide (III) were dissolved in 40 mL DIW under stirring. Then, the clear orange solution stayed at 140 °C for 6 h. With the same procedures as disposing of Ni–Co PBA precursors, the maroon precipitates of Fe–Fe PB precursors were got. Finally, heating these precursors in air at 450 °C for 3 h, the Fe_2O_3 microleaves were obtained.

Material Characterization: The surface morphologies of the as-obtained materials were characterized by the FESEM (JSM-7800F) and TEM (JEOL-2100F). The surface area and crystal structures of the materials were investigated by the BET (Quadrasorb 2MP) and XRD (Bruker D8 Advance X-ray diffractometer). The elemental mapping images of the as-obtained materials were obtained from the EDX. XPS (ESCALAB250Xi) was used to investigate the surface chemical states and composition of the products. Nitrogen sorption measurement was performed on Autosorb 6B at liquid N_2 temperature.

Electrochemical Measurements: The working electrodes were prepared as the following steps: 1) mixing 80 wt% of active materials with 10 wt% of binder polytetrafluoroethylene (PTFE) and 10 wt% conductive agent (super-P-Li); 2) coating the obtained slurry on a nickel foam surface with a mass loading around 3 mg cm^{-2}; 3) drying the as-prepared electrodes in the oven for 6 h, then the working electrodes were prepared. A three-electrode measurement equipment was constructed coupled with a counter electrode (Pt foil) and a reference electrode (Hg/HgO). 3 M potassium hydroxide aqueous solution was used as the electrolyte. Both the cyclic voltammetry (CV) and galvanostatic charge–discharge (GCD) studies were performed on a CHI 660E electrochemical workstation. The electrochemical impedance spectroscopy (EIS) was obtained on a Zahner IM6 electrochemical workstation. The cycling life was conducted on a LAND battery system.

Fabrication of EC Devices: The electrochemical capacitor was fabricated by using the obtained NiO/Co_3O_4 microcubes as the cathode and Fe_2O_3 microleaves as the anode, a glass fiber paper was employed as the diaphragm in 3 M KOH electrolyte. To obtain the optimal performance, the mass loading of anode and cathode was decided by the equation: $m+/m_- = C_- * \Delta V_- / C+ * \Delta V+$. By calculation, the mass loading of NiO/Co_3O_4 microcubes and Fe_2O_3 microleaves were ≈4.12 and 3 mg cm^{-2}, respectively. The specific energy density (E) and power density (P) of the EC device were obtained through the equations: $E = 1/2C(V)^2$, $P = E/t$, where C, V, and t are the specific capacitance, working potential, and discharge time of the EC device respectively. All the related electrochemical tests were performed in the two-electrode test system.

Fabrication of Solar-Charging Power Stations: To verify the feasibility of our designed EC device as an efficient solar charging power station, a xenon lamp (PLS-SXE300) was used as the simulation photosource to irradiate three series monocrystalline silicon plates (CNC 55 × 55 1.5 V), the as-prepared electrochemical capacitor was connected with the monocrystalline silicon plates in parallel.

Supporting Information

Supporting Information is available from the Wiley Online Library or from the author.

Acknowledgements

X.W. and W.H. contributed equally to this work. This work was supported by the graduate research and innovation foundation of Chongqing (Grant No. CYS18050).

Conflict of Interest

The authors declare no conflict of interest.

Keywords

electrochemical capacitors, energy density, MOF derivatives, solar charging

Received: May 6, 2019
Revised: May 28, 2019
Published online: June 12, 2019

[1] Z. Wen, M. H. Yeh, H. Y. Guo, J. Wang, Y. L. Zi, C. G. Hu, Z. L. Wang, *Sci. Adv.* **2016**, *2*, e1600097.
[2] G. Nagaraju, S. C. Sekhar, B. Ramulu, L. K. Bharat, G. S. R. Raju, Y. K. Han, J. S. Yu, *Nano Energy* **2018**, *50*, 448.
[3] Y. Shabangoli, M. S. Rahmanifar, M. F. El-Kady, A. Noori, M. F. Mousavi, R. B. Kaner, *Energy Storage Mater.* **2018**, *11*, 282.
[4] P. Thounthong, V. Chunkag, P. Sethakul, S. Sikkabut, S. Pierfederici, B. Davat, *J. Power Sources* **2011**, *196*, 313.
[5] M. A. B. Fathallah, A. B. Othman, M. Besbes, *Appl. Phys. A* **2018**, *124*, 120.
[6] A. Das, S. Deshagani, R. Kumar, M. Deepa, *ACS Appl. Mater. Interfaces* **2018**, *10*, 35932.
[7] F. C. Zhou, Z. W. Ren, Y. D. Zhao, X. P. Shen, A. W. Wang, Y. Y. Li, C. Surya, Y. Chai, *ACS Nano* **2016**, *10*, 5900.
[8] W. L. Jing, C. H. Lai, W. S. H. Wong, M. L. D. Wong, *Appl. Energy* **2018**, *224*, 340.
[9] S. Li, Y. Chen, Q. Xiang, M. K. Aslam, B. B. Hu, W. Li, Y. Tang, Q. Yu, Y. P. Liu, C. G. Chen, *J. Mater. Chem. A* **2019**, *7*, 1658.
[10] Y. O. Yang, R. J. Huang, X. F. Xia, H. T. Ye, X. Y. Jiao, L. Wang, W. Lei, Q. L. Hao, *Chem. Eng. J.* **2019**, *355*, 416.
[11] D. P. Zhao, H. Q. Liu, X. Wu, *Nano Energy* **2019**, *57*, 363.
[12] G. Wee, T. Salim, Y. M. Lam, S. G. Mhaisalkar, M. Srinivasan, *Energy Environ. Sci.* **2011**, *4*, 413.
[13] M. G. Li, W. W. Yang, J. Li, M. Feng, W. L. Li, H. B. Li, Y. S. Yu, *Nanoscale* **2018**, *10*, 2218.
[14] J. H. Lin, H. H. Wang, Y. T. Yan, X. H. Zheng, H. N. Jia, J. L. Qi, J. Cao, J. C. Tu, W. D. Fei, J. C. Feng, *J. Mater. Chem. A* **2018**, *6*, 19151.
[15] X. J. Wei, H. R. Peng, Y. H. Li, Y. B. Yang, S. H. Xiao, L. Peng, Y. H. Zhang, P. Xiao, *ChemSusChem* **2018**, *11*, 3167.
[16] X. D. Liu, G. M. Sheng, M. L. Zhong, X. W. Zhou, *Nanoscale* **2018**, *10*, 4209.
[17] X. J. Wei, H. R. Peng, Y. H. Li, M. Zhou, Y. H. Zhang, P. Xiao, *Chem. Eng. J.* **2018**, *341*, 618.
[18] L. Ni, R. W. Wang, H. B. Wang, C. Y. Sun, B. Sun, X. Guo, S. Jiang, Z. Q. Shi, W. D. Jing, L. K. Zhu, S. L. Qiu, Z. T. Zhang, *Carbon* **2018**, *139*, 1152.
[19] M. Vijayakumar, J. Adduru, T. N. Rao, M. Karthik, *Global Challenges* **2018**, *2*, 1800037.
[20] D. P. Dubal, O. Ayyad, V. Ruiz, P. G. Romero, *Chem. Soc. Rev.* **2015**, *44*, 1777.
[21] B. Y. Guan, A. Kushima, L. Yu, S. Li, J. Li, X. W. Lou, *Adv. Mater.* **2017**, *29*, 1605902.
[22] S. D. Liu, Y. Yin, M. Wu, K. S. Hui, K. N. Hui, C. Y. Ouyang, S. C. Jun, *Small* **2018**, *15*, 1803984.
[23] H. R. Peng, B. Yao, X. J. Wei, T. Y. Liu, T. Y. Kou, P. Xiao, Y. H. Zhang, Y. Li, *Adv. Energy Mater.* **2019**, *9*, 1803665.
[24] J. H. Lin, Z. X. Zhong, H. H. Wang, X. H. Zhang, Y. H. Wang, J. L. Qi, J. Cao, W. D. Fei, Y. D. Huang, J. C. Feng, *J. Power Sources* **2018**, *407*, 6.
[25] X. J. Xu, J. Liu, Z. B. Liu, J. D. Shen, R. Z. Hui, J. W. Liu, L. Z. Ouyang, L. Zhang, M. Zhu, *ACS Nano* **2017**, *11*, 9033.
[26] J. X. Zhao, Y. Zhang, X. X. Zhao, R. T. Wang, J. X. Xie, C. F. Yang, J. J. Wang, Q. C. Zhang, L. L. Li, C. H. Lu, Y. G. Yao, *Adv. Funct. Mater.* **2019**, https://doi.org/10.1002/adfm.201900809.
[27] M. Hu, A. A. Belik, M. Imura, K. Mibu, Y. Tsujimoto, Y. Yamauchi, *Chem. Mater.* **2012**, *24*, 2698.
[28] J. G. Wang, Z. Y. Zhang, X. Y. Zhang, X. M. Yin, X. Li, X. R. Liu, F. Y. Kang, B. Q. Wei, *Nano Energy* **2017**, *39*, 647.
[29] J. J. Li, X. X. Yan, X. Y. Li, X. H. Zhang, J. H. Chen, *Talanta* **2018**, *179*, 726.
[30] B. Kong, X. T. Sun, C. Selomulya, J. Tang, G. F. Zheng, Y. Q. Wang, D. Y. Zhao, *Chem. Sci.* **2015**, *6*, 4029.
[31] C. X. Wang, L. W. Yin, L. Y. Zhang, Y. X. Qi, N. L, N. N. Liu, *Langmuir* **2010**, *26*, 12841.
[32] E. Nossol, *Adv. Funct. Mater.* **2009**, *19*, 3980.
[33] B. Y. Guan, X. Y. Yu, H. B. Wu, X. W. Lou, *Adv. Mater.* **2017**, *29*, 1703614.
[34] P. H. Zhou, D. S. Xue, H. Q. Luo, X. G. Chen, *Nano Lett.* **2002**, *2*, 845.
[35] L. Li, L. Tan, G. N. Li, Y. M. Zhang, L. L. Liu, *Langmuir* **2017**, *33*, 12087.
[36] N. Yan, L. Hu, Y. L, Y. Wang, H. Zhong, X. Y. Hu, X. K. Kong, Q. W. Chen, *J. Phys. Chem. C* **2012**, *116*, 7227.
[37] L. Zhang, H. B. Wu, S. Madhavi, H. H. Hng, X. W. Lou, *J. Am. Chem. Soc.* **2012**, *134*, 17388.
[38] X. J. Wei, Y. H. Li, H. R. Peng, D. Gao, Y. H. Zhang, P. Xiao, *Chem. Eng. J.* **2019**, *355*, 336.
[39] J. G. Kim, D. L Pugmire, D. Battaglia, M. A. Langell, *Appl. Surf. Sci.* **2000**, *165*, 70.
[40] K. Wang, J. Yang, J. X. Zhu, L. Li, Y. Liu, C. Zhang, T. X. Liu, *J. Mater. Chem. A* **2017**, *5*, 11236.
[41] A. Shanmugavani, R. K. Selvan, *Electrochim. Acta* **2016**, *189*, 283.
[42] S. E. Moosavifard, S. Fani, M. Rahmanianc, *Chem. Commun.* **2016**, *52*, 4517.
[43] M. Wang, M. Pyeon, Y. Gonullu, A. Kaouk, S. H. Shen, L. J. Guo, S. Mathur, *Nanoscale* **2015**, *7*, 10094.
[44] H. A. Bandal, A. R. Jadhav, A. A. Chaugule, W. J. Chung, H. Kim, *Electrochim. Acta* **2016**, *222*, 1316.
[45] C. Zhang, J. Xiao, X. L. Lv, L. H. Qian, S. L. Yuan, S. Wang, P. X. Lei, *J. Mater. Chem. A* **2016**, *4*, 16516.
[46] Y. Z. Zhang, Y. Wang, Y. L. Xie, T. Chen, W. Y. Lai, H. Pang, W. Huang, *Nanoscale* **2015**, *6*, 14354.
[47] Y. Huan, H. W. Wang, Y. T. Jing, T. Q. Peng, X. F. Wang, *J. Power Sources* **2015**, *285*, 281.
[48] Y. Wang, Z. X. Chen, T. Lei, Y. F. Ai, Z. K. Peng, X. Y. Yan, H. Li, J. J. Zhang, Y. L. Chueh, *Adv. Energy Mater.* **2018**, *8*, 1870076.
[49] Y. G. W. Yan, F. Song, Y. Y. Xia, *Chem. Soc. Rev.* **2016**, *45*, 5232.
[50] R. Wang, Y. W. Sui, S. F. Huang, Y. G. Pu, P. Cao, *Chem. Eng. J.* **2018**, *331*, 527.
[51] T. Liu, L. Y. Zhang, W. You, J. G. Yu, *Small* **2018**, *14*, 1702407.
[52] S. W. Zhang, B. S. Yin, Z. B. Wang, F. Peter, *Chem. Eng. J.* **2016**, *306*, 193.
[53] L. Q. Mai, F. Yang, Y. L. Zhao, X. X. Lin, L. Xu, Y. Z. Luo, *Nat. Commun.* **2011**, *2*, 503.
[54] Q. F. Wang, X. F. Wang, B. Liu, G. Yu, X. J. Hou, D. Chen, G. Z. Shen, *J. Mater. Chem. A* **2013**, *1*, 2468.
[55] Q. Lu, M. W. Lattanzi, Y. P. Chen, X. M. Kou, W. F. Li, X. Fan, K. M. Unruh, J. G. G. Chen, J. Q. Xiao, *Angew. Chem.* **2011**, *123*, 6979.
[56] R. R. Salunkhe, J. Tang, Y. Kamachi, T. Nakato, J. H. Kim, Y. Yamauchi, *ACS Nano* **2015**, *9*, 6288.
[57] G. L. Sun, H. Y. Xie, J. B. Ran, L. Y. Ma, X. Y. Shen, J. M. Hu, H. Tong, *J. Mater. Chem. A* **2016**, *4*, 16576.
[58] S. W. Zhang, B. S. Yin, C. Liu, Z. B. Wang, D. M. Gu, *Chem. Eng. J.* **2017**, *312*, 296.
[59] Q. Q. Tang, W. Q. Wang, G. C. Wang, *J. Mater. Chem. A* **2015**, *3*, 6662.
[60] J. J. Li, M. C. Liu, L. B. Kong, D. Wang, Y. M. Hu, W. Han, L. Kang, *RSC Adv.* **2015**, *5*, 41721.
[61] J. Z. Chen, J. L. Xu, S. Zhou, N. Zhao, C. P. Wong, *Nano Energy* **2016**, *21*, 145.
[62] W. K. Zhang, B. Zhao, Y. L. Yin, T. Yin, J. Y. Cheng, K. Zhan, Y. Yan, J. H. Yang, J. Q. Li, *J. Mater. Chem. A* **2016**, *4*, 19026.
[63] J. X. Zhu, L. Huang, Y. X. Xiao, L. Shen, Q. Chen, W. Z. Shi, *Nanoscale* **2014**, *6*, 6772.
[64] C. Guan, W. Zhao, Y. T. Hu, Z. C. Lai, X. Li, S. J. Sun, H. Zhang, A. K. Cheetham, J. Wang, *Nanoscale Horiz.* **2017**, *2*, 99.
[65] H. L. Wang, Q. M. Gao, J. Hu, *J. Power Sources* **2010**, *195*, 3017.
[66] P. Wen, P. W. Gong, J. F. Sun, J. Q. Wang, S. R. Yang, *J. Mater. Chem. A* **2015**, *3*, 13874.